scientific reports

Check for updates

OPEN

# Thermally assisted microbot transport through high-viscosity media

A. K. Ishiki[1], K. B. Neeves[2,3] & D. W. M. Marr[1]✉

**Many potential in vivo microbot (μbot) applications require transport through high-viscosity environments. We have previously demonstrated that rotating magnetic fields can be used to reversibly assemble and drive μbots composed of paramagnetic microparticles. In this, particle surface chemistry can be readily manipulated and the combination of chemical degradation and mechanical action used to enhance penetration of μbot swarms into gelled networks. Here we show that a thermal approach, created through a hyperthermia-induced heating of microparticles with complementary alternating magnetic fields, can also be used to enhance mechanical action by lowering local viscosity. In addition, we observe that a rapid μbot back and forth sweeping motion induced by the applied field significantly improves penetration rates by reducing both μbot size and viscous resistance.**

Microscale devices, known as μbots, can be actuated and controlled though external magnetic,[1,2] acoustic,[3] and electric[4] fields for applications in the blood stream[5,6] such as targeted drug delivery[7,8] and blood clot clearance[9,10]. To extend their use to the respiratory system, gastrointestinal tract, and eyes, μbots must transport through highly viscous mucus for effective use. In previous studies, microparticle-based approaches have shown promise when used passively with enhanced diffusion in high-viscosity systems[11]. Active μbots assembled from similar particles may further address the challenges of such viscous environments by providing additional mechanical[12] forces, chemically-induced[13] degradation or, as we investigate here, heating to alter the local viscosity at scales associated with μbot transport. In previous work, we have demonstrated the use of rotating magnetic fields (RMFs) for the assembly of superparamagnetic microparticles into μbots that roll like wheels[14] and capable of climbing up steep inclines,[15] altering direction based on polymer concentration,[16] and translating across air-water interfaces[17]. These rolling μbots have demonstrated enhanced penetration through and degradation of fibrin-based networks when functionalized with tissue plasminogen activator in both in vitro[18,19] and in vivo studies[20,21]. By now applying an external high-frequency alternating magnetic field (AMF), microparticles containing nm-scale iron oxide domains can be heated via hyperthermia. While the RMF changes direction continuously to produce steady rotational motion, the AMF rapidly oscillates direction along a single axis. In this, the AMF leads to internal friction through rapid realignment of magnetic moments within particles resulting in increased temperatures[22].

Because magnetic hyperthermia is non-invasive[23], it has been used and shown effective in destroying carcinogenic cells[24] by rapidly increasing temperatures[25] of iron-based nanoparticles to a therapeutic range (41–46 ˚C), and it has also been utilized to enhance controlled drug release[26]. Additionally, hyperthermic particles have been incorporated into μbot superstructures using internal heat generation to alter its structure to adapt to variable confinement scales[27]. Here, we investigate the use of hyperthermia for enhancing μbot transport by applying an AMF for particle heating (Fig. 1A) while using a separate RMF for μbot assembly and translation (Fig. 1B). To demonstrate this principle we choose a model system composed of gelatin whose viscous properties arise from its collagen sourced material,[28] forming a temperature-dependent entangled network analogous to mucus, where large polymeric mucin glycoproteins[29] lead to high viscosities. With this we show that hyperthermic heating can lower μbot transport resistance from viscous media for significantly faster penetration (Fig. 1C).

[1]Department of Chemical and Biological Engineering, Colorado School of Mines, Golden, CO, USA. [2]Department of Bioengineering, University of Colorado Denver, Anschutz Medical Campus, Aurora, CO, USA. [3]Department of Pediatrics, University of Colorado Denver, Anschutz Medical Campus, Aurora, CO, USA. ✉email: dmarr@mines.edu

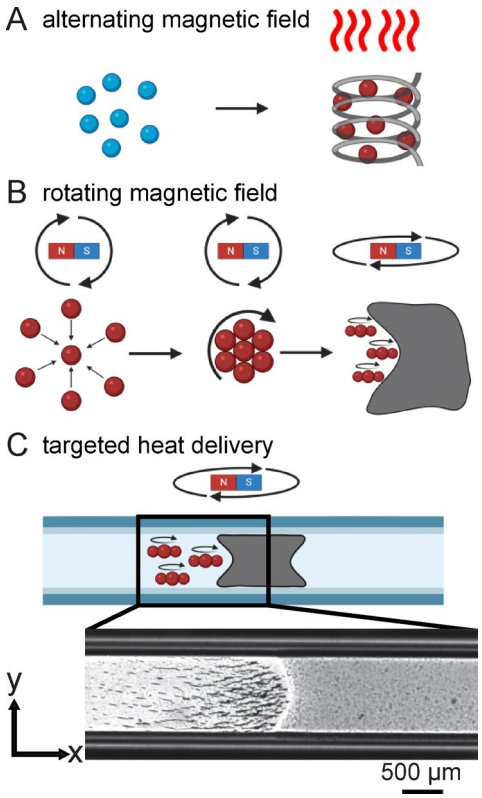


**Fig. 1**. (**A**) µBot components, initially at room temperature (blue), heated (red) with an AMF. (**B**) µBots assembled and translated using an RMF. (**C**) Heated µbots (left) penetrating viscous media (right).

## Results and discussion

Temperature can strongly influence viscosity; for example, a change from 20 ˚C to 30 ˚C results in an ~ 20% decrease in water viscosity[30]. Polymeric solution viscosities can exhibit even stronger changes with temperature[31] where dilute polyethylene-based solutions can experience a ~ 60% viscosity drop with a 10 ˚C temperature rise[32]. In biological systems, large polymeric molecules[33,34] form adhesive interactions though chain entanglement, van der Waals forces, and hydrogen bonding[35,36]. As temperature increases, van der Waals forces and hydrogen bonding weaken while the interconnected gel network loosens and becomes more flexible, resulting in reduced viscosity. Gastropod mucus for example shows order of magnitude changes over a temperature change of ~ 5 ˚C[37]. Here, we choose gelatin for experimental convenience and because it derives its viscous properties from polymeric proteins, in the form of collagen[28] in the case of gelatin and glycoproteins[29] in the case of mucin. Similar to mucus, gelatin melts with a viscosity drop at ~ 20 ˚C over a comparable temperature change (Fig. 2A). Following the phase transition, gelatin viscosity steadily decreases as temperature continues to rise, a behavior also observed in various types biological media such as blood[38], synovial fluid[39], saliva and mucus[40]. For a solution containing 5 mg of particles in 1 ml of water and subjected to 30 min of AMF heating, the solution temperature rises above 24 ˚C (Fig. 2B), the melting temperature of 4% gelatin (gel-24) (Fig. 2A), but only approach the melting temperature of 5% gelatin (gel-25) (Fig. 2A) from ambient conditions ~ 20 ˚C. We verify this with penetration experiments without the RMF (Fig. 3A) where there is a clear indication that gel-24 was penetrated with heat independent of mechanical action from the RMF. Gel-25 had no noticeable changes, which shows that particles were able to reach a temperature between 24 and 25 ˚C.

Because we have chosen particles for easy manipulation, they are optimized for their paramagnetic and not their hyperthermic properties. Nanoparticles, not dissimilar to those embedded within the polystyrene matrix we use here, have been shown to reach temperatures of ~ 70 ˚C in cancer studies[25]. In these systems, heating efficiency is a strong function of magnetic nanoparticle size, shape, crystallinity, and composition; for spherical iron oxide based particles, the optimal size is ~ 15 nm[41]. The microparticles used here are composed of a polystyrene matrix containing ~ 20% iron oxide of domain size ~ 8 nm[42] with these smaller domains reducing heating efficiency[43]. The larger encapsulating microparticles, however, both allow the generation of greater mechanical forces and can reduce iron oxide exposure to the surrounding environment. Given this, we use a field strength of ~ 50 mT for heat generation, higher than typical field strengths used in clinical trials[44,45] (1–20 mT) and significantly higher than the fields required for µbot assembly and translation (~ 3 mT). As a result, we apply the AMF and RMF sequentially to heat and manipulate µbots over multiple cycles (see "Methods and Materials"). Due to practical constraints, imaging was performed during the manipulation step. For efficient hyperthermic heating of micro- and nanoparticles, frequencies on the order of ~ 100 kHz are generally needed[46] which is much higher than the ~ 30 Hz frequencies used for the RMF. We also note that the larger particle

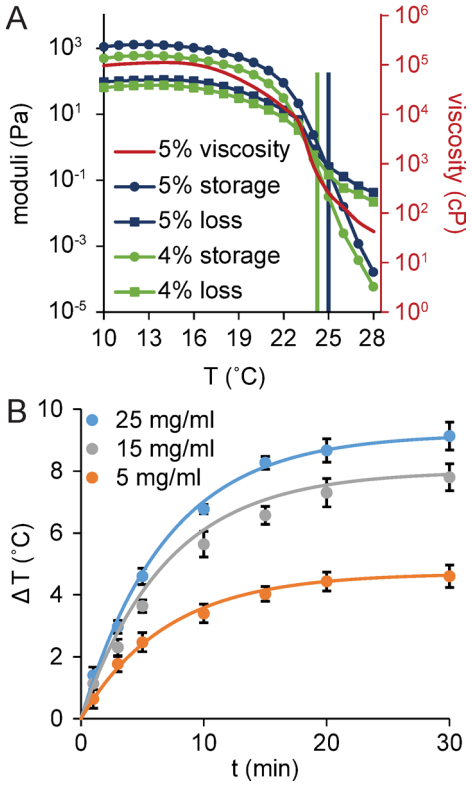


**Fig. 2**. (**A**) Viscosity, storage modulus, and loss modulus of 4% and 5% gelatin decreases with temperature. The vertical green (gel-24) and dark-blue (gel-25) lines indicate the melting temperature. (**B**) Temperature of magnetic particle solutions of varying concentration under AMF heating rises over time. Fit follows the AMF heating model (Eq. 3).

system provides greater force and larger shear at the frequencies we manipulate them. The greater mechanical forces can be especially relevant in biological media, where viscosity can be reduced substantially under high shear conditions. Many biological fluids exhibit shear-thinning behaviors[47], where mechanical disruption can significantly reduce viscosity. We estimate the stress μbots exert on the viscous gelatin interface with the shear rate which is on the order of $\dot{\gamma} = V_e/R \sim 1\ s^{-1}$, where $V_e$ is the μbot edge velocity and $R$ the μbot radius. This shear rate is sufficient to produce enough mechanical stress during translation to effectively lower viscosity over an order of magnitude from a rested state (Supplemental Fig. 1). Consequently, higher RMF strengths could enhance μbot mechanical force and work synergistically with hyperthermic heating, further lowering the viscosity of shear-thinning environments.

Even with larger particles, individual μbots are limited by their cargo carrying capacity. To increase loading, μbots can be manipulated as swarms[48] with different application-specific modes[15]. Rolling mode for example is simple in that there are no changes to heading direction or camber angle (Fig. 3B). This mode builds the largest μbots and achieves the fastest speed. Due to the accumulation of particles at the viscous interface however, normal rolling mode is not effective as μbots agglomerate into sizes too large to effectively roll within physical limitations of the capillary tube (Supplementary Movie 1). This is a potential issue for certain airways[49] and blood vessels[50] that can be even smaller (< 1 mm). To address this, we employ corkscrew mode which follows a helical path and has been shown effective at penetrating into and degrading fibrin-based gels[18]. Corkscrew mode however is limited at high particle concentrations where μbots are drawn towards the swarm centroid into large formations that struggle to translate forward and penetrate the viscous media. Switchback mode has a constant camber angle and rapid back-and-forth changes to heading direction useful for inclines. The rapid changes to heading direction break up larger μbots into smaller components capable of penetrating with a rate $V$ of 0.7 ± 0.21 μm/s (Supplementary Movie 2). Compared to corkscrew mode, the directional changes are much faster which minimizes the time allowed for μbots to attract and combine with one another leading to steady forward translation and penetration into the heated gelatin. In previous studies, we have observed that μbots can climb inclines[15] up to 80° making it likely that, at the front interface, they briefly roll up to the top surface; however, these μbots would fall immediately back and be reincorporated into the swarm due to gravity.

The highest velocities are observed when heat is combined with the mechanical disruption of switchback mode. We decouple these effects by investigating mechanical disruption, heat conduction, and heat convection independently (see "Methods and Materials"). For mechanical disruption, the μbot swam is driven towards the gelatin interface for penetration without AMF heating, conduction involves heating the particle solution without RMF manipulation, and convection uses AMF heating for the particle solution and RMF manipulation to direct the swarm back and forth near the interface but does not drive towards it. Without AMF, mechanical disruption

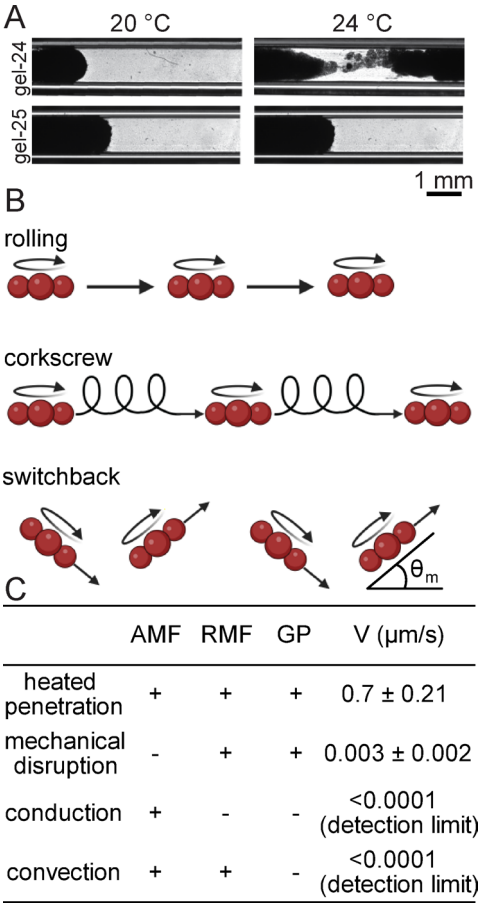


| | AMF | RMF | GP | V (μm/s) |
|---|---|---|---|---|
| heated penetration | + | + | + | 0.7 ± 0.21 |
| mechanical disruption | - | + | + | 0.003 ± 0.002 |
| conduction | + | - | - | <0.0001 (detection limit) |
| convection | + | + | - | <0.0001 (detection limit) |

**Fig. 3**. (**A**) Magnetic particle solutions (left) heating gelatins (right) of different melting temperatures with AFM and no RMF translation. (**B**) Swarm mode translation paths. $\theta_m$ is the switchback mode maximum turn angle. (**C**) Decoupled effects of μbot heating and translation on gelatin penetration rates $V$ ($n = 10$). GP = directed towards gelatin penetration.

by itself has a significantly slower $V$ with the gelatin near its highest viscosity with a high storage modulus (Fig. 2A). By using either no RMF or without an AMF but employing a modified switchback mode, we determine that there are no measurable changes for the cases of conduction and convection. As the particle solution gets warmer, the structural strength of the gelatin weakens which can be seen from the decreasing viscosity (Fig. 2A). However, the viscous interface remains unchanged without active disruption from mechanical forces even with mixing effects from convection performed here. The hyperthermia-induced heating of the particle solution has a gradual temperature rise over 30 min, providing ample time for the particle solution and interface temperatures to equilibrate. With a negligible temperature difference, convection does not provide any improvement to conduction and does not show any changes to the viscous interface with thermal action alone. We determine that the mechanism of efficient penetration involves mechanical disruption from the rapid sweeping motion of switchback mode to physically clear viscous media softened through AMF heating of μbots.

Smooth μbot swarm translation during switchback mode is achieved through fragmenting μbots into smaller components. A swarm composed of numerous smaller μbots better samples the surface for weaker regions and provides a greater number of penetration points along the viscous interface. The direction change frequency of switchback mode $\omega_{sb}$ can be varied to reduce average μbot size and increase the penetration speed. The critical breakup frequency can be estimated by balancing the magnetic and viscous torques acting upon μbots during switchback turning $T = T_m + T_v = 0$. To determine the magnetic torque, we start with the potential energy $U = -\boldsymbol{m} \bullet \boldsymbol{B} = -mBcos(\varphi)$ μbots acquire from the external field of magnitude $B$ where $m = N\frac{4}{3}\pi a^3 \mu_0 \chi B$ is the induced magnetic moment, $\varphi$ the angle between the magnetic field and the μbot dipole alignment, $N$ the number of particles composing a μbot, $a$ the particle radius, $\mu_0$ the magnetic permeability of free space, and $\chi$ the magnetic susceptibility. Assuming that the slower dipole relaxation time scale induces a phase lag between the μbot alignment and the external field[51], the magnetic torque is determined via[52]

$$T_m = -\frac{dU}{d\varphi} = -N\frac{4}{3}\pi a^3 \mu_0 \chi B^2 sin(\varphi), \quad (1)$$

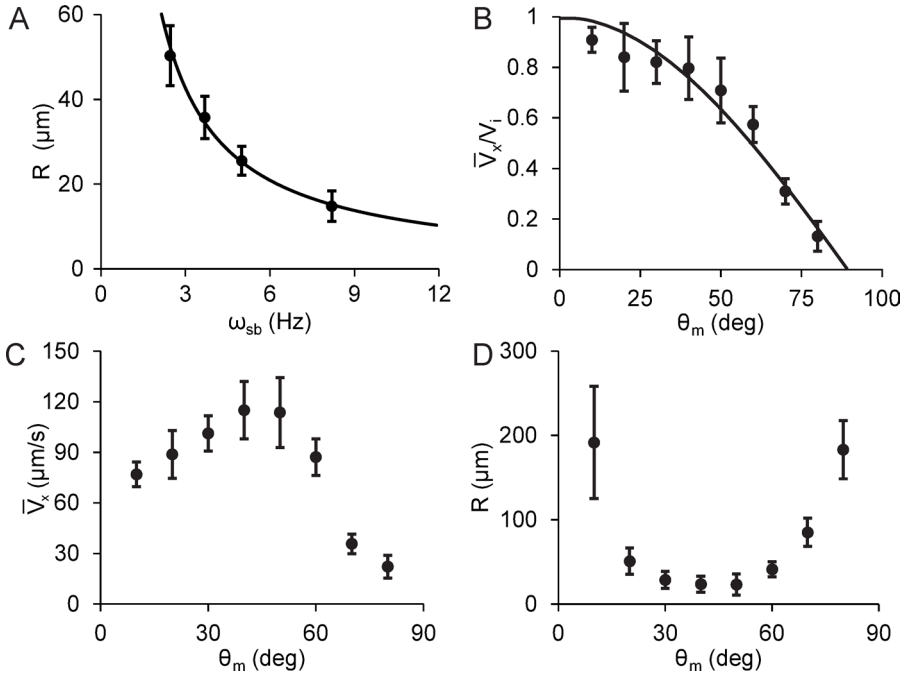


**Fig. 4**. (**A**) μBot radius decreases as turn frequency increases at a 35˚ turn angle. Fit follows $\omega_{sb} \propto R^{-1}$. (**B**) Average x-velocity for dispersed individual μbots normalized by the instantaneous velocity decreases as turn angle increases. Fit follows Eq. (9). (**C**) High particle concentration μbot swarm x-velocity initially increases with turn angle, reaching a maximum at ~45˚, before decreasing again. (**D**) μBot radius initially decreases with increasing turn angle, reaching a minimum at ~45˚, before increasing again.

that is balanced with the lateral viscous torque[53] $T_v = \frac{16}{3}\eta\,\omega_{sb}R^3$ to determine an expression for the critical breakup frequency

$$\omega_{sb} = \frac{N\pi\, a^3 \mu_0 \chi\, B^2 sin\,(\varphi)}{4\eta\, R^3}. \tag{2}$$

Assuming 2D hexagonal close packing of particles, $N \propto R^2$ and we expect $\omega_{sb} \propto R^{-1}$ at constant magnetic field strength. This is indeed observed experimentally when increasing $\omega_{sb}$ as μbots do break up into smaller components (Fig. 4A). As the turn frequency increases, stronger viscous resistance from the aqueous environment results in a more aggressive breakup.

In addition to turn frequency, the maximum turn angle $\theta_m$ (Fig. 3B) influences μbot swarm translation. We track the average μbot velocity in the forward x-direction $\bar{V}_x$ for a system without gelatin. For a dispersed system with a 100x diluted particle concentration where μbot-μbot interactions are negligible, $\bar{V}_x/V_i$ decreases with increasing $\theta_m$ (Eq. 9, Fig. 4B); however, at higher particle concentrations needed for useful AMF heating, $\bar{V}_x$ instead increases with $\theta_m$ (Fig. 4C). To clarify the role of μbot-μbot interactions, we drive the swarm back and forth while maintaining the centroid position (Supplemental Fig. 2A). Here, these interactions, as indicated by significant spreading of the swarm mass, propel the front of the swarm forward at higher $\bar{V}_x$ with swarm spreading increasing with particle concentration (Supplemental Fig. 2B). A maximum occurs at ~45˚ before $\bar{V}_x$ begins to drop (Fig. 4C). We also observe that μbot size decreases with $\theta_m$, reaching a minimum at ~45˚ before increasing in size again. The $\bar{V}_x$ maximum and $R$ minimum both occur at ~45˚ due to the turn path during switchback mode. When $\theta_m \leq 45^\circ$, μbots maintain a horizontal orientation during the turn where the leading μbot edges are facing forward. For $\theta_m > 45^\circ$, the leading edge switches to the opposite side for each direction change, resulting in a shorter turn angle without pointing directly forward in the x-direction (Supplementary Movie 3). At ~45˚, μbot-μbot interactions in the x-direction are the strongest leading to a $\bar{V}_x$ maximum.

Higher turn frequencies $\omega_{sb}$ lead to higher $\bar{V}_x$ (Fig. 5A) and, as a result, $V$ increases with both $\theta_m$ and $\omega_{sb}$. Taking advantage of μbot interactions, the fastest penetration rate is achieved at 45˚ and 14 Hz (Fig. 5B); however, penetration rates drop significantly as $\theta_m$ exceeds 45˚. As previously mentioned, interactions between the leading edge of μbots and the viscous interface lowers for $\theta_m > 45^\circ$. Gelatin exhibits shear-thinning

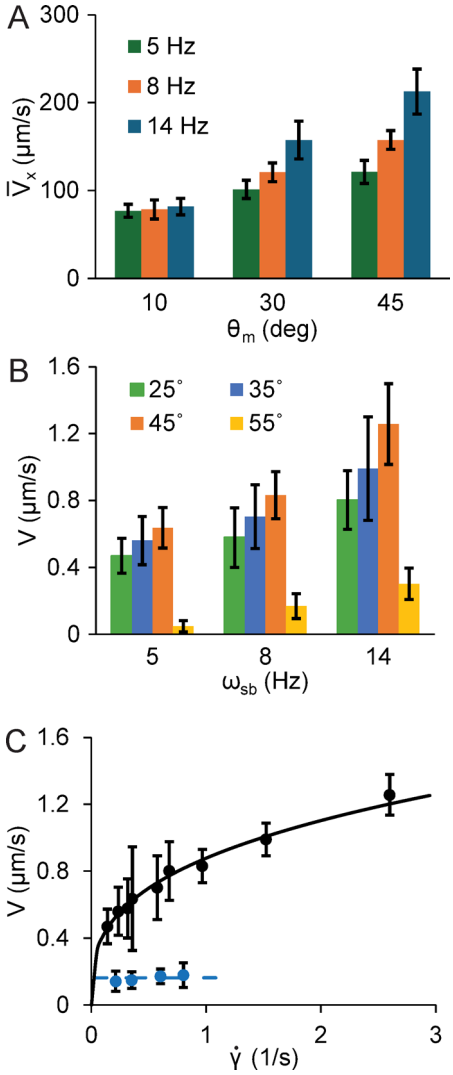


**Fig. 5**. (**A**) Average µbot swarm forward velocity increases with turn angle and frequency. (**B**) Heated µbot gelatin penetration rate increases with turn frequency, reaching a maximum at ~45˚, before decreasing again. (**C**) Gelatin penetration rate increases with shear rate. Blue points indicate measurements in glycerol. Black fit line follows the power-law fluid model and blue dashed line fit follows the Newtonian case.

behavior and the reduction of mechanical disruption could inhibit shear-thinning effects, resulting in a drop to penetration rate. To determine shear-thinning contributions during viscous media penetration, we look at $V$ in relation to the shear rate that µbots create.

We model the relationship between viscosity and shear rate $\dot{\gamma}$ as a power-law fluid[54] with $\eta \propto \dot{\gamma}^{n-1}$, where $n$ is the power-law index. The power-law index quantifies the fluid's deviation from Newtonian behavior where $n = 1$ correlates to a Newtonian fluid, $n < 1$ is shear-thinning, and $n > 1$ is shear-thickening. For similar µbot sizes, rotation rates, and magnetic field strengths, the µbot rotation rate $\omega_r \propto 1/\eta$ by balancing[16] the induced magnetic torque with the rotational drag for a thin disk[55]. Further, balancing the frictional force and the laminar edge-wise drag on a disk[56] yields $\bar{V}_x \propto 1/\eta$, where $\bar{V}_x$ is equivalent to the µbot swarm velocity $V$ during viscous media penetration as verified with measurements in glycerol solutions (Supplemental Fig. 3). Substituting for viscosity results in $V \propto \dot{\gamma}^{1-n}$. Here, we estimate and manipulate shear rate using the µbot edge velocity during switchback turning by varying $\omega_{sb}$. In the Newtonian case where $n = 1$ (Fig. 5C), we expect that $V$ remains constant with $\dot{\gamma}$ which is consistent with measurements in glycerol but deviates in the non-Newtonian case with gelatin. Fitting the data to the power-law fluid model gives $n = 0.67 \pm 0.10$ further supported by rheometer measurements yielding $n = 0.54 \pm 0.02$ (Supplemental Fig. 1). This suggests significant shear-thinning behavior[57] under stress exerted by the µbot swarm.

For applications involving viscous biological media, there will be significant challenges to efficient transport. Here we have demonstrated a heating-based approach that is both non-invasive and complementary to other readily implemented methods with µbots assembled from colloidal particles. We anticipate that, for specific applications, field-induced heating will be one component of an overall approach that can take advantage of

chemical and mechanical methods as well. For example, iron oxide nanoparticles have shown potential in a co-therapeutic approach combining thermal and chemotherapeutic effects for targeted cancer cell treatment[58]. While increasing temperature can lower viscosity, hydration also plays a key role; for instance, a common characteristic of diseased mucus is a reduction in water content[47]. Note that a particle-based delivery approach is compatible with nebulizer-based misting strategies for delivery to the lungs where particles could be suspended and delivered in aqueous droplets[59]. Combined with mucoactive agents[60] and thermally enhanced diffusion, mucus viscosity could be further lowered with swarm modes to enhance μbot induced mixing.

## Conclusions

We investigate the use of field-induced hyperthermia with magnetic μbot swarms to enhance the penetration of μbot swarms through high-viscosity media. Our work demonstrates that both thermal softening and mechanical disruption are simultaneously required for effective penetration. In this, μbot heating lowers local viscosity while an additional field-induced sweeping motion can be used to enhance penetration. Higher rates are achieved at higher turn frequencies and an optimal turn angle of 45˚ by breaking down μbots into smaller components and enhancing the velocity into the viscous interface. Through this combination of thermal and mechanical means, μbot transport can be enhanced within highly viscous media.

## Methods and materials

### Gel preparation and characterization

Gelatin derived from tilapia skin (O'crème kosher fish gelatin) was prepared by mixing with 0.2% sodium dodecyl sulfate (SDS) (Sigma-Aldrich) on low heat overnight with 1% gel food color (blue, Betty Crocker) added for imaging contrast. Small amplitude oscillatory shear temperature sweeps from 10 to 28 ˚C at 1% strain and 1 rad/s were performed with an AR-G2 rheometer (TA Instruments) with a 2˚ 60 mm cone-and-plate geometry. Storage modulus, loss modulus, and viscosity were measured with the gelatin melting temperature identified as the crossover of loss and storage modulus (Fig. 2B).

### Calorimetry

Three solutions of 4.5 μm superparamagnetic polystyrene particles containing ~ 20% iron oxide[42] (Dynabeads 450-Epoxy, Thermo Fischer), purchased at an initial concentration of ~ $4{\cdot}10^8$ particles $ml^{-1}$, were prepared with 0.2% SDS at concentrations of 5, 15, and 25 mg/ml. 1 ml of each particle solution was placed in a separate 1.5 ml Eppendorf tube and then insulated within a 50 ml centrifuge tube lined with polystyrene foam sealed with the tube cap. To quantify heating, calorimetry was performed at an AMF (U.S. Solid, USS-HFIH00001-220 V) frequency of ~ 70 kHz. In this, the sample was placed in the AMF coil ensuring that the Eppendorf tube was at the coil center. Each temperature measurement started at room temperature (~ 20 ˚C). The temperature profile[61] of the particle solutions under AMF heating was modeled as

$$T(t) = \Delta T_{max} e^{\frac{-thA}{C}} + T_0, \tag{3}$$

where $T$ is the temperature, $t$ the heating duration, $\Delta T_{max}$ the maximum measured temperature change, $h$ the free convection heat transfer coefficient, $A$ the particle surface area ~ $4.2 \cdot 10^{-3}$ $m^2$, $C = \sum C_{p,\,i} m_i$ the weighted-summed specific heats in solution 4.19 $\frac{J}{kg\,K}$ with $C_{p,\,i}$ the specific heat, $m_i$ the mass, and $T_0$ the initial temperature. Equation (3) was fit with the temperature data (Fig. 2B) to get an estimate for $h$ ~2 $\frac{W}{m^2 K}$. The specific adsorption rate[61] (SAR) for a particle concentration of 5 mg/ml or ~$6.5 \times 10^7$ particles/ml was determined to be 9.96 ± 0.38 W/g from

$$SAR = \frac{hA\Delta T_{max}}{m_p}, \tag{4}$$

where $m_p$ is the mass of particles with a power per particle of ~ $7.2 \times 10^{-10}$ W/particle. For particle concentrations of 15 and 25 mg/ml, the SAR was 5.58 ± 0.43 and 3.56 ± 0.45 W/g, respectively, which is expected as SAR decreases at higher particle concentration due to dipole-dipole interactions interfering with Néel relaxation[62]. All error calculations were ± 1 standard deviation. We estimate the relevant heat transfer time scales, based on a simple lumped system analysis (Biot number $Bi = hr/3k \sim 10^{-3}$ where $r$ is the particle radius $2.25 \times 10^{-6}$ $m$, and $k$ the thermal conductivity 0.035 $\frac{W}{m\,K}$), to determine the rate at which particles lose heat to the aqueous environment. In this analysis, heat retention timescales are determined from $\rho\, LC_{p,\,b}/h$ ~ 0.1 s, where $\rho$ is the particle density 1600 $\frac{kg}{m^3}$ and $C_{p,\,p}$ the average particle specific heat ~ 1100 $\frac{J}{kg\,K}$.

### Penetration and translation studies

Gelatin penetration experiments were performed in 2.5 in long glass square capillary tubes with an inner width of 1 mm (VitroCom). The center of the tube was filled with a 4% ("gel-24") or 5% ("gel-25") gelatin solution at 35 ˚C and cooled to room temperature. Due to capillary action and liquid adhesive forces to the wall, a parabolic interface forms. ~0.03 ml of 5 mg/ml particle solution was filled on one side of the gelatin and the other side filled with ~ 0.03 ml of DI water. This particle concentration was used for all experiments unless otherwise specified. Both ends of the tube were sealed with tacky wax (Collecting Warehouse) and particles concentrated at the gelatin interface with a permanent magnet. A small piece of tape was placed on top of the capillary tube near the center as reference for penetration rate measurements. Particle and gelatin heating with the AMF was verified with 4% and 5% gelatin samples heating for 30 min in the AMF coil with the particle mass-gelatin interface

placed at the center of the coil. For experiments using the RMF, only 5% gelatin was used since it remains in a solid-like state (G' > G" where G' is the storage modulus and G" the loss modulus) under elevated temperature conditions. Glycerol solutions were prepared by mixing glycerol (The Science Company) in 0.2% SDS overnight.

The RMF is output with a 5-coil system, one for the z axis and two for each of the x and y axes. Each coil is 50 mm i.d. 400 turns incorporated onto a microscope stage (Olympus OpenStand). The generated RMF is defined as

$$\boldsymbol{B}(t) = \begin{cases} B_x = B\cos(\omega_f t) \\ B_y = B\cos(\omega_f t - \frac{\pi}{2}) \\ B_z = B\cos(\omega_f t - \varphi_z) \end{cases} \tag{5}$$

where $\omega_f$ is the angular field frequency and $\varphi_z$ the phase angle. The RMF was kept at a field strength of ~ 3 mT, rotating frequency of 30 Hz, maximum turn angle of 35°, and switchback frequency of 8 Hz using homebuilt software[63] unless otherwise specified. Image analysis for µbot tracking was performed with ImageJ. Due to low heat retention, gelatin penetration required repeated cycles of a heating phase followed by a translation phase. In the heating phase, the sample tube was placed in the AMF coil for 30 min, then transferred (< 5 s) to the microscope stage where the translation phase with the RMF for 90 s was applied and repeated to measure penetration rate. RMF coil-induced heating was quantified by replacing the sample with a temperature probe. Experiments involving the rotating magnetic field were kept under 2 min where measured coil-induced temperature changes were negligible.

To investigate conduction, a gelatin capillary tube sample was prepared with magnetic particles. The sample was heated with an AMF, but no RMF translation was used. For convection, the sample was heated with an AMF and a RMF used to induce switchback mode translation but was not directed for gelatin penetration. µBots were driven back and forth near the gelatin interface by alternating the net-forward direction between the positive and negative x-direction to induce mixing without interacting directly with the interface. For mechanical disruption, no AMF was used. Only the RMF was used for switchback mode translation and directed towards the gelatin interface for penetration.

### µBot swarm modes and switchback velocity model

µBot swarm modes are identified by the pattern of their heading direction $\theta$ and camber angle $\theta_c$ at constant RMF strength and frequency. For rolling mode, both heading direction angle and camber angle are held constant. Corkscrew mode includes gradual changes to both heading direction and camber angle with heading direction defined as

$$\theta(t) = \frac{2\pi}{t_t} t, \tag{6}$$

and camber angle as

$$\theta_c(t) = \begin{cases} \theta_{c,max}\left(\frac{2t}{t_t}\right), & 0 \le t \le \frac{t_t}{2} \\ \theta_{c,max}(2 - \frac{2t}{t_t}), & \frac{t_t}{2} < t \le t_t \end{cases} \tag{7}$$

where $t_t \approx 1\ s$ is the duration of a single turn and $\theta_{c,max} = 50^\circ$ the maximum camber angle. In switchback mode, the forward component of the µbot velocity is $V_x = V_i \cos(\theta)$, with $V_i$ the instantaneous µbot velocity. In this $\theta$ is defined as

$$\theta(t) = \begin{cases} \pm\theta_m \cos\left(\frac{\pi}{t_t} t\right), & 0 \le t \le t_t \\ \theta_m, & t_t < t \le t_c \end{cases} \tag{8}$$

where $\theta_m$ is the maximum heading direction angle, $t_t \approx 0.05\ s$, and $t_c$ is the total duration of a single turn and the waiting period before the next turn combined. Assuming constant $V_i$, the average forward velocity $\bar{V}_x$ can be expressed as

$$\frac{\bar{V}_x}{V_i} = \frac{t_t \frac{\sin(\theta_m)}{\theta_m} + (t_c - t_t)\cos(\theta_m)}{t_c}. \tag{9}$$

## Data availability

Raw datasets generated during this study are available from the corresponding author upon reasonable request.

Received: 8 October 2025; Accepted: 16 December 2025
Published online: 19 December 2025

## References

1. Abbott, J. J., Diller, E. & Petruska, A. J. Magnetic methods in robotics. *Annu. Rev. Control Robot Auton. Syst.* **3**, 57–90 (2020).
2. Chen, X. Z. et al. Recent developments in magnetically driven micro- and nanorobots. *Appl. Mater. Today*. **9**, 37–48 (2017).
3. Xiao, Y., Zhang, J., Fang, B., Zhao, X. & Hao, N. *Acoustics-Actuated Microrobots Micromachines* **13**, 481 (2022).

4. Kim, H. & Kim, M. J. Electric field control of Bacteria-Powered microrobots using a static obstacle avoidance algorithm. *IEEE Trans. Robot.* **32**, 125–137 (2016).
5. Nelson, B. J., Kaliakatsos, I. K. & Abbott, J. J. Microrobots for minimally invasive medicine. *Annu. Rev. Biomed. Eng.* **12**, 55–85 (2010).
6. Doutel, E. & Galindo-Rosales, F. J. Campo-Deaño, L. Hemodynamics challenges for the navigation of medical microbots for the treatment of CVDs. *Materials* **14**, 7402 (2021).
7. Hu, M. et al. Micro/Nanorobot: A promising targeted drug delivery system. *Pharmaceutics* **12**, 665 (2020).
8. Jang, D., Jeong, J., Song, H. & Chung, S. K. Targeted drug delivery technology using untethered microrobots: a review. *J. Micromech Microeng.* **29**, 053002 (2019).
9. Yang, M. et al. Swarming magnetic nanorobots bio-interfaced by heparinoid-polymer brushes for in vivo safe synergistic thrombolysis. *Sci. Adv.* **9**, eadk7251 (2023).
10. Wang, S. et al. Accelerating thrombolysis using a precision and clot-penetrating drug delivery strategy by nanoparticle-shelled microbubbles. *Sci. Adv.* **6**, eaaz8204 (2020).
11. Lai, S. K. et al. Rapid transport of large polymeric nanoparticles in fresh undiluted human mucus. *Proc. Natl. Acad. Sci. U.S.A.* 104, 1482–1487 (2007).
12. Aghakhani, A. et al. High shear rate propulsion of acoustic microrobots in complex biological fluids. *Sci. Adv.* **8**, eabm5126 (2022).
13. Walker, D., Käsdorf, B. T., Jeong, H. H., Lieleg, O. & Fischer, P. Enzymatically active biomimetic micropropellers for the penetration of mucin gels. *Sci. Adv.* **1**, e1500501 (2015).
14. Tasci, T. O., Herson, P. S., Neeves, K. B. & Marr, D. W. M. Surface-enabled propulsion and control of colloidal microwheels. *Nat. Commun.* **7**, 10225 (2016).
15. Zimmermann, C. J., Herson, P. S., Neeves, K. B. & Marr, D. W. M. Multimodal microwheel swarms for targeting in three-dimensional networks. *Sci. Rep.* **12**, 5078 (2022).
16. Ishiki, A. K., Neeves, K. B. & Marr, D. W. M. Reversible microwheel translation induced by polymer depletion. *Langmuir* **39**, 15547–15552 (2023).
17. Wolvington, E., Yeager, L., Gao, Y., Zimmermann, C. J. & Marr, D. W. M. Paddlebots: translation of rotating colloidal assemblies near an Air/Water interface. *Langmuir* **39**, 7846–7851 (2023).
18. Tasci, T. O. et al. Enhanced fibrinolysis with magnetically powered colloidal microwheels. *Small* **13**, 1700954 (2017).
19. Disharoon, D., Trewyn, B. G., Herson, P. S., Marr, D. W. M. & Neeves, K. B. Breaking the fibrinolytic speed limit with microwheel co-delivery of tissue plasminogen activator and plasminogen. *J. Thromb. Haemost.* **20**, 486–497 (2022).
20. Pontius, M. H. H. et al. Magnetically powered microwheel thrombolysis of occlusive thrombi in zebrafish. *Proc. Natl. Acad. Sci. U.S.A.* 121, e2315083121 (2024).
21. Osmond, M. J. et al. Micrometer-scale tPA beads amplify plasmin generation for enhanced thrombolytic therapy. *Bioeng. Transla Med.* e70012 (2025). https://doi.org/10.1002/btm2.70012
22. Ota, S. & Takemura, Y. Characterization of Néel and brownian relaxations isolated from complex dynamics influenced by dipole interactions in magnetic nanoparticles. *J. Phys. Chem. C.* **123**, 28859–28866 (2019).
23. Joshi, R., Jadhao, M. & Ghosh, S. K. Recent trends in the applications of nanocomposites in cancer theranostics. *Green. Sustainable Process. Chem. Environ. Eng. Sci.* (Elsevier), 283–320. https://doi.org/10.1016/B978-0-323-95169-2.00011-0 (2023).
24. Koleoso, M. et al. Micro/nanoscale magnetic robots for biomedical applications. *Mater. Today Bio.*. **8**, 100085 (2020).
25. Rajan, A. & Sahu, N. K. Review on magnetic nanoparticle-mediated hyperthermia for cancer therapy. *J. Nanopart. Res.* **22**, 319 (2020).
26. Park, J., Jin, C., Lee, S., Kim, J. & Choi, H. Magnetically actuated degradable microrobots for actively controlled drug release and hyperthermia therapy. *Adv. Healthc. Mater.* **8**, 1900213 (2019).
27. Landers, F. C. et al. On-Command disassembly of microrobotic superstructures for transport and delivery of magnetic micromachines. *Adv. Mater.* **36**, 2310084 (2024).
28. Rajabimashhadi, Z., Gallo, N., Salvatore, L. & Lionetto, F. Collagen derived from fish industry waste: progresses and challenges. *Polymers* **15**, 544 (2023).
29. Wagner, C. E., Wheeler, K. M. & Ribbeck, K. Mucins and their role in shaping the functions of mucus barriers. *Annu. Rev. Cell. Dev. Biol.* **34**, 189–215 (2018).
30. Korson, L., Drost-Hansen, W. & Millero, F. J. Viscosity of water at various temperatures. *J. Phys. Chem.* **73**, 34–39 (1969).
31. Kol, R. et al. Toward more universal prediction of polymer solution viscosity for Solvent-Based recycling. *Ind. Eng. Chem. Res.* **61**, 10999–11011 (2022).
32. Al-Shammari, B., Al-Fariss, T., Al-Sewailm, F. & Elleithy, R. The effect of polymer concentration and temperature on the rheological behavior of metallocene linear low density polyethylene (mLLDPE) solutions. *J. King Saud Univ. - Eng. Sci.* **23**, 9–14 (2011).
33. Harding, S. E. The intrinsic viscosity of biological macromolecules. Progress in measurement, interpretation and application to structure in dilute solution. *Prog. Biophys. Mol. Biol.* **68**, 207–262 (1997).
34. de la García, J. & Hernández Cifre, J. G. Hydrodynamic properties of biomacromolecules and macromolecular complexes: concepts and Methods. A tutorial Mini-review. *J. Mol. Biol.* **432**, 2930–2948 (2020).
35. Liu, M., Zhang, J., Shan, W. & Huang, Y. Developments of mucus penetrating nanoparticles. *Asian J. Pharm. Sci.* **10**, 275–282 (2015).
36. Ponchel, G. Specific and non-specific bioadhesive particulate systems for oral delivery to the Gastrointestinal tract. *Adv. Drug Deliv. Rev.* **34**, 191–219 (1998).
37. Hanlon, D. F., Clouter, M. J. & Andrews, G. T. Temperature dependence of the viscoelastic properties of a natural gastropod mucus by Brillouin light scattering spectroscopy. *Soft. Matter.*. **19**, 8101–8111 (2023).
38. Çinar, Y. Blood viscosity and blood pressure: role of temperature and hyperglycemia. *Am. J. Hypertens.* **14**, 433–438 (2001).
39. Hasnain, S. et al. Knee synovial fluid flow and heat transfer, a power law model. *Sci. Rep.* **13**, 18184 (2023).
40. Penconek, A., Michalczuk, U., Sienkiewicz, A. & Moskal, A. The effect of desert dust particles on rheological properties of saliva and mucus. *Environ. Sci. Pollut Res.* **26**, 12150–12157 (2019).
41. Gavilán, H. et al. Magnetic nanoparticles and clusters for magnetic hyperthermia: optimizing their heat performance and developing combinatorial therapies to tackle cancer. *Chem. Soc. Rev.* **50**, 11614–11667 (2021).
42. Fonnum, G., Johansson, C., Molteberg, A., Mørup, S. & Aksnes, E. Characterisation of Dynabeads® by magnetization measurements and Mössbauer spectroscopy. *J. Magn. Magn. Mater.* **293**, 41–47 (2005).
43. Shah, R. R. et al. Determining iron oxide nanoparticle heating efficiency and elucidating local nanoparticle temperature for application in agarose gel-based tumor model. *Mater. Sci. Engineering: C.* **68**, 18–29 (2016).
44. Liu, X. et al. Comprehensive Understanding of magnetic hyperthermia for improving antitumor therapeutic efficacy. *Theranostics* **10**, 3793–3815 (2020).
45. Johannsen, M. et al. Clinical hyperthermia of prostate cancer using magnetic nanoparticles: presentation of a new interstitial technique. *Int. J. Hyperth.* **21**, 637–647 (2005).
46. Kouzoudis, D., Samourgkanidis, G., Kolokithas-Ntoukas, A., Zoppellaro, G. & Spiliotopoulos, K. Magnetic hyperthermia in the 400–1,100 kHz frequency range using mions of condensed colloidal nanocrystal clusters. *Front. Mater.* **8**, 638019 (2021).
47. Lai, S. K., Wang, Y. Y., Wirtz, D. & Hanes, J. Micro- and macrorheology of mucus. *Adv. Drug Deliv. Rev.* **61**, 86–100 (2009).
48. Yang, L. & Zhang, L. Motion control in magnetic microrobotics: from individual and multiple robots to swarms. *Annu. Rev. Control Robot Auton. Syst.* **4**, 509–534 (2021).

49. Seneterre, E., Paganin, F., Bruel, J., Michel, F. & Bousquet, J. Measurement of the internal size of bronchi using high resolution computed tomography (HRCT). *Eur. Respir J.* **7**, 596–600 (1994).
50. Bosetti, F. et al. Small Blood Vessels: Big Health Problems? Scientific Recommendations of the National Institutes of Health Workshop. *JAHA* 5, e004389 (2016).
51. Cunha, L. H. P. et al. Slow relaxation dynamics of superparamagnetic colloidal beads in time-varying fields. *Phys. Rev. Mater.* **8**, 105601 (2024).
52. Erb, R. M., Martin, J. J., Soheilian, R., Pan, C. & Barber, J. R. Actuating soft matter with magnetic torque. *Adv. Funct. Mater.* **26**, 3859–3880 (2016).
53. Kanwal, R. P. Slow rotatory motion of a circular disk about one of its diameters in a viscous fluid. *J. Appl. Mech.* **26**, 485–487 (1959).
54. Bird, R. B., Stewart, W. E. & Lightfoot, E. N. *Transport Phenomena* (Wiley, 2002).
55. Jeffery, G. B. On the steady rotation of a solid of revolution in a viscous fluid. *Proc. Lond. Math. Soc.* **s2_14**, 327–338 (1915).
56. Tanzosh, J. P. & Stone, H. A. Transverse motion of a disk through a rotating viscous fluid. *J. Fluid Mech.* **301**, 295–324 (1995).
57. Martínez-Padilla, L. P. Rheology of liquid foods under shear flow conditions: recently used models. *J. Texture Stud.* **55**, e12802 (2024).
58. Serio, F. et al. Co-loading of doxorubicin and iron oxide nanocubes in Polycaprolactone fibers for combining Magneto-Thermal and chemotherapeutic effects on cancer cells. *J. Colloid Interface Sci.* **607**, 34–44 (2022).
59. Zimmermann, C. J. et al. Delivery and actuation of aerosolized microbots. *Nano Select Nano*. **202100353** https://doi.org/10.1002/nano.202100353 (2022).
60. Balsamo, R., Lanata, L. & Egan, C. G. Mucoactive drugs. *Eur. Respir Rev.* **19**, 127–133 (2010).
61. Andreu, I. & Natividad, E. Accuracy of available methods for quantifying the heat power generation of nanoparticles for magnetic hyperthermia. *Int. J. Hyperth.* **29**, 739–751 (2013).
62. Deatsch, A. E. & Evans, E. E. Heating efficiency in magnetic nanoparticle hyperthermia. *J. Magn. Magn. Mater.* **354**, 163–172 (2014).
63. Zimmermann, C. czimm79/MuControl: v1.1.1 - DOI generation. *Zenodo* https://doi.org/10.5281/ZENODO.5793922 (2021).


## Acknowledgements

The authors acknowledge support from the National Institutes of Health under Grant Nos. R21AI138214 and R01NS102465 and the Colorado Office of Economic Development and International Trade grant #CTGG12025-2438. Figures 1 and 3B were created with BioRender.com.

## Author contributions

D.W.M.M. and K.B.N. conceived the ideas and obtained financial support. A.K.I. performed the experiments and the data analysis. A.K.I. and D.W.M.M. designed the work and wrote the initial paper draft. All authors contributed to and edited the final version of the manuscript.

## Funding

The authors acknowledge support from the National Institutes of Health under Grant Nos. R21AI138214 and R01NS102465 and the Colorado Office of Economic Development and International Trade grant #CTGG12025-2438.

## Declarations

## Competing interests

The authors declare no competing interests.

## Additional information

**Supplementary Information** The online version contains supplementary material available at https://doi.org/10.1038/s41598-025-33125-0.

**Correspondence** and requests for materials should be addressed to D.W.M.M.